Dielectric function and double absorption onset of monoclinic Cu2SnS3

Origin of experimental features explained by first-principles calculations

Crovetto, Andrea; Chen, Rongzhen; Ettlinger, Rebecca Bolt; Cazzaniga, Andrea Carlo; Schou, Jørgen; Persson, Clas; Hansen, Ole

Published in:
Solar Energy Materials & Solar Cells

Link to article, DOI:
10.1016/j.solmat.2016.04.028

Publication date:
2016

Document Version
Peer reviewed version

Dielectric function and double absorption onset of monoclinic Cu_2SnS_3: origin of experimental features explained by first-principles calculations

Andrea Crovetto[a,*], Rongzhen Chen[b], Rebecca Bolt Ettlinger[c], Andrea Carlo Cazzaniga[c], Jørgen Schou[c], Clas Persson[b,d], Ole Hansen[a,e,**]

[a] *DTU Nanotech, Technical University of Denmark, DK-2800 Kgs. Lyngby, Denmark*
[b] *Department of Materials Science and Engineering, Royal Institute of Technology, SE-100 44 Stockholm,Sweden*
[c] *DTU Fotonik, Technical University of Denmark, DK-4000 Roskilde, Denmark*
[d] *Department of Physics, University of Oslo, P.O. Box 1048 Blindern, NO-0316 Oslo, Norway*
[e] *CINF, Center for Individual Nanoparticle Functionality, Technical University of Denmark, Technical University of Denmark, DK-2800 Kgs. Lyngby, Denmark*

Abstract

In this work, we determine experimentally the dielectric function of monoclinic Cu_2SnS_3 (CTS) by spectroscopic ellipsometry from 0.7 to 5.9 eV. An experimental approach is proposed to overcome the challenges of extracting the dielectric function of Cu_2SnS_3 when grown on a glass/Mo substrate, as relevant for photovoltaic applications. The ellipsometry measurement reveals a double absorption onset at 0.91 eV and 0.99 eV. Importantly, we demonstrate that calculation within the density functional theory (DFT) confirms this double onset only when a very dense **k**-mesh is used to reveal fine details in the electronic structure, and this can explain why it has not been reported in earlier calculated spectra. We can now show that the double onset originates from optical transitions at the Γ-point from three energetically close-lying valence bands to a single conduction band. Thus, structural imperfection, like secondary phases, is not needed to explain such an absorption spectrum. Finally, we show that the absorption coefficient of CTS is particularly large in the near-band gap spectral region when compared to similar photovoltaic materials.

Keywords:
CTS, Cu_2SnS_3, optical properties, band gap, ellipsometry

1. Introduction

The ternary chalcogenide semiconductor Cu_2SnS_3 (CTS) has attracted interest as a solar cell absorber material in the last half decade. Indeed, promising power conversion efficiencies of 4.63% and 4.29% have recently been reported by two independent groups [1, 2]. The main potential advantage of CTS over quaternary absorbers Cu(In,Ga)Se_2 (CIGS), Cu_2ZnSnS_4 (CZTS), and $Cu_2ZnSnSe_4$ (CZTSe) is a relatively broad single-phase region and reduced fabrication complexity due to fewer chemical constituents [3]. Furthermore, the CTS compound consists of inexpensive and non-toxic chemical elements, unlike the common high-efficiency chalcogenide absorbers CIGS and CdTe. CTS is typically produced by high temperature sulfurization of metal precursors [1] or of a precursor S-containing compound [2, 3].

Depending on the deposition parameters and sulfurization conditions, CTS can form with different crystal structures. Tetragonal, cubic, monoclinic, and triclinic phases have been reported. Despite such phase variety, a theoretical work [4] has shown that all the commonly observed crystal structures are based on the same zincblende pattern with tetrahedral coordination. The only difference between them is the degree of disorder in the cation sublattice, which results in different crystal symmetries. The monoclinic phase is a perfectly ordered phase, whereas the disordered cubic and tetragonal phases feature different arrangements of tetrahedral S-Cu_2Sn_2 and S-Cu_3Sn structural motifs. The best-performing CTS solar cells reported so far had a CTS absorber with monoclinic structure [1, 2].

A double absorption onset of 0.90-0.93 eV and 0.97-1.02 eV [1, 5, 6] has consistently been reported in the literature for monoclinic CTS, on the basis of both optical absorption and quantum efficiency (QE) measurements. It has been shown [7] that the double onset is an intrinsic feature of monoclinic CTS and it does not arise from other CTS phases or other compounds. However, another study [8] has shown that a disordered structure can exist locally even in single-phase monoclinic CTS due to the high density of structural defects such as stacking faults, which modify the local atomic coordination. This leaves the open question of whether the double onset is a feature of defect-free monoclinic CTS, or if it is a consequence of the high defect density found in CTS thin films, which locally alters its band structure and consequently its optical transitions. While the electronic structure and density-of-states of monoclinic CTS have earlier been analyzed theoretically [4, 9, 10, 11] and the optical properties have been computed [4, 9], the double onset

*Corresponding author, email: ancro@nanotech.dtu.dk, Ørsteds Plads, building 345 East, DK-2800 Kgs. Lyngby, Denmark, Tel.: +45 4525845
**Principal corresponding author, email: ole.hansen@nanotech.dtu.dk, Ørsteds Plads, building 345 East, DK-2800 Kgs. Lyngby, Denmark, Tel.: +45 4525715

phenomenon was not reported in those studies. Furthermore, no experimental data on the dielectric function of monoclinic CTS is found in the literature. Experimental dielectric functions have only been reported for multi-phase films identified as a mix of tetragonal and cubic CTS [12], where it is not possible to isolate the dielectric functions of the two single phases.

In this work, we synthesize thin films of monoclinic CTS by pulsed laser deposition (PLD) on Mo-coated glass in order to reproduce the conditions under which CTS is formed in solar cell devices. We extract the complex dielectric function $\varepsilon(E) = \varepsilon_1(E) + i\varepsilon_2(E)$ of CTS in the photon energy range from $E = 0.7$ to 5.9 eV by spectroscopic ellipsometry measurement, and compare it to the dielectric function calculated within the density functional theory (DFT) to corroborate the results and to investigate the origin of the double onset phenomenon. We find that the very details in the dielectric response at the band-gap energy are revealed only with a very dense **k**-point sampling. Then, the double onset phenomenon is explained as optical transitions from the three topmost bands at the valence band maximum (VBM) in a perfectly crystalline CTS. Thus, the phenomenon does not need to be due to structural imperfections, like a disordered structure or secondary phases. Also, with the dense **k**-mesh the shapes of both the real and imaginary parts of the dielectric function are improved considerably in the low energy region (i.e., below 1.5 eV).

2. Experimental details

Thin films of Mo (approximately 500 nm thick) were deposited on soda lime glass (SLG) by DC magnetron sputtering, with a sputtering pressure of 1.3×10^{-2} mbar for the first 200 nm (adhesion layer) and 3.9×10^{-3} mbar for the last 300 nm (low-resistivity layer).

Thin films of Cu_2SnS_3 were deposited at room temperature on Mo-coated soda lime glass substrates in a pulsed laser deposition (PLD) setup with a background pressure below 3×10^{-6} mbar. The substrates were cleaned sequentially by ultrasonic treatment for 5 minutes in acetone and isopropanol and finally rinsed in ultrapure water. The laser beam from a Nd:YAG laser (355 nm wavelength, 7 ns pulse duration) with a repetition rate of 10 Hz was partly focused onto a beam-spot of 2.2 mm^2 with an angle of incidence of 45° with respect to the target normal and a target-substrate distance of 4.4 cm, as illustrated in Fig. 1. The laser fluence was set to 1.6 J/cm^2. The targets used are sintered power disks provided by Testbourne Ltd with the stoichiometry Cu_2SnS_3.

After deposition, the samples were annealed at 570°C for 10 minutes in a sealed furnace evacuated down to 10^{-4} mbar and then filled with 100 mbar of N_2 gas. Samples were placed in a graphite box in the hot zone of the furnace together with 160 mg of sulfur.

The films were imaged with a scanning electron microscope (SEM) equipped with a field emission gun (FE-SEM, Supra 60VP, Zeiss). Energy dispersive X-ray spectroscopy (EDX) was performed in the same instrument using a silicon drift detector (X-Max^N 50, Oxford Instruments) and a beam voltage of 15 kV. EDX spectra were taken on five different spots and averaged. The error bars are expressed as the standard deviation of the measurements. The EDX analysis software (AzTec, Oxford Instruments) was calibrated with elemental standards instead of with a reference compound. Therefore, we expect the standard error due to an oversimplified EDX spectrum analysis to be larger than the standard deviation of the measurements.

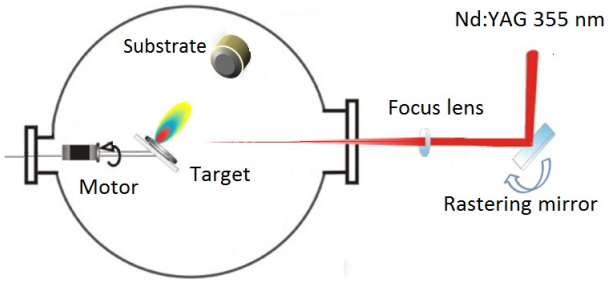

Figure 1: Scheme of the pulsed laser deposition setup. In a vacuum chamber a pulsed laser source (Nd:YAG, 355 nm, 7 ns pulses at 10 Hz) is focused onto a target, which is ablated by the laser. The combination of target rotation and a rastering mirror ensures uniform ablation of the target.

X-ray diffraction (XRD) patterns were collected with a Bruker D8 powder diffractometer in Bragg-Brentano configuration using Cu-K_α radiation, a 0.009° step size, and a 1.5 s/step integration time. In order to avoid possible peak shifts due to sample alignment errors, the diffraction pattern was aligned using the peaks of standard Si powder.

Raman spectra were obtained in the backscattering configuration at a laser wavelength of 455 nm and laser power of 1.6 mW, using a 50× objective that resulted in a spot size of about 2 μm × 2 μm (DXR Raman Microscope, Thermo Scientific).

Ellipsometry measurements were performed in reflection mode in the spectral range 0.7-5.9 eV on a rotating compensator spectroscopic ellipsometer (M-2000, J.A. Woollam Co.) using a collimated beam with a spot size of approximately 200 μm × 300 μm. Ellipsometry spectra were analyzed and fitted with the CompleteEase software package (version 5.06 - J.A. Woollam Co.). When properties of a thin film are to be extracted by an ellipsometry measurement, the reliability of the results depends strongly on the amount of unknown fitting parameters, versus the number of independent measured variables that can be used to fit such parameters [13]. In order to increase the number of measured variables, we measured the magnitude ($\tan\Psi$) and phase (Δ) of the ratio between p- and s- type polarization reflection coefficients for six angles of incidence (from 45 to 70° in steps of 5°), giving twelve measured variables at each wavelength, which were fitted simultaneously in the data analysis step. In order to decrease the number of fitting parameters, we extracted the dielectric function of each layer independently in a separate ellipsometry measurement, as explained in the following sections. A Kramers-Kronig-consistent b-spline model was used to model the shape of the dielectric functions, as demonstrated previously [14]. This means that the imaginary part $\varepsilon_2(E)$ was fitted by a b-spline function using control points spaced by 0.2 eV, whereas the real part $\varepsilon_1(E)$ was not fitted independently but was instead derived by Kramers-Kronig

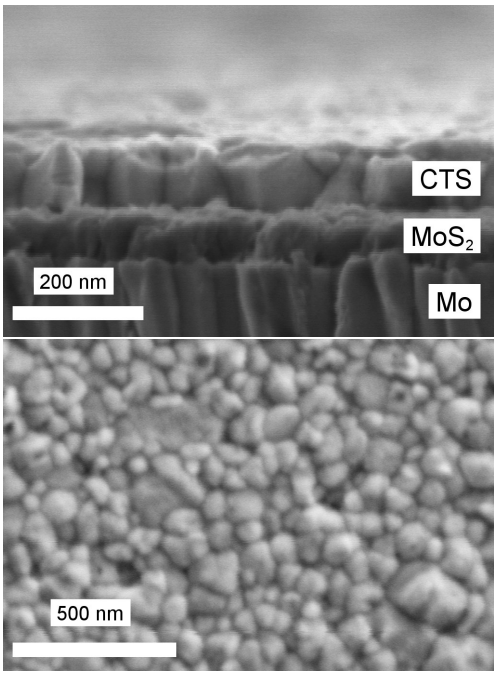

Figure 2: Cross-sectional and top-view SEM images of the annealed CTS films on a glass/Mo/MoS_2 stack. The Mo, MoS_2 and CTS layers are clearly visible and are labeled in the cross-sectional image. Each film covers the underlying layers uniformly without obvious pinholes or intermixing. From the cross-sectional image, the estimated film thicknesses are 80 nm for the MoS_2 layer and 100 nm for the CTS layer.

integration. This implies that the relation between $\varepsilon_1(E)$ and $\varepsilon_2(E)$ is a physical one, and that one fitting parameter, instead of two, is required at each control point. Bruggeman's effective medium theory [13] was employed to treat surface roughness as a 50%-solid-film-50%-air layer. Unless otherwise stated, the thickness of the films and of the surface roughness layer were treated as unknown parameters and fitted in the model. However, in order to constrain their range to realistic values and reduce potential correlation errors, their initial values were assigned on the basis of measurements done with other techniques. Since all the layers of interest for this study can be clearly identified in cross sectional SEM images (Fig. 2), pixel counting from high-resolution SEM images allowed us to estimate film thicknesses. In the case of surface roughness, the measurement was done by atomic force microscopy (AFM) in tapping mode over a 2 μm $\times$ 2 μm area (Bruker Dimension Icon). The measured root-mean-square roughness value (R_q) was used to initialize the thickness of the surface roughness layer in the ellipsometry model (R_e), because a good correlation between the two quantities has been observed before, following the empirical formula $R_e \approx 1.5\,R_q + 4$ Å [15]. When fitting ellipsometry data, the allowed range for thickness and roughness values was then restricted to the estimated value ±20%.

3. Computational details

The electronic and dielectric responses are theoretically analyzed by means of the plane augmented wave formalism within the DFT as implemented in the VASP program package [16, 17]. We model the monoclinic Cu_2SnS_3 crystal with a 12 atom base-centered primitive cell, space group $Cc = C_s^4$ with unique axis b. The electron density and the optical properties are described with the exchange-correlation potential by Heyd et al. (HSE06) [18] using a $K = 5\times5\times5$ Γ-centered Monkhorst-Pack like **k**-mesh which implies $N_k = 39$ **k**-points in the irreducible Brillouin zone (IBZ). We use the standard mixing and range-separation parameter for HSE06. With these parameters, the estimated error bar of the band gap energy for similar compounds is about 0.1-0.2 eV [19, 20]. All the calculations are performed with an energy cutoff of 420 eV. The structure of monoclinic CTS (4a site atom positions) is fully relaxed using the HSE06 potential until the total energy and the residual force on each atom converge to 0.1 meV and 10 meV/Å, respectively. The relaxed lattice parameters of the monoclinic CTS are a = 6.67 Å, b = 11.57 Å, c = 6.68 Å, and β = 109.41° for unique axis b, obtained with the HSE06 exchange-correlation potential with the standard parameter setting.

The imaginary part $\varepsilon_2(E)$ of the dielectric function is computed directly from the electronic structure and the optical matrix elements performing a tetrahedron integration, while the real part $\varepsilon_1(E)$ is obtained via the Kramers-Kronig transformation, similarly to the experimental approach.

In addition, we perform complementary calculations using the generalized gradient approximation (i.e., PBE [21]) and the PBE+U approach [22] with an onsite Coulomb interaction of U_d(Cu) = 6 eV on the Cu d-like orbitals. PBE implies zero gap energy. With the correction potential U_d(Cu), the energy gap is opened slightly and the d-like energy states are also corrected [23]. However, an additional constant upwards shift of the conduction band minimum (CBM) of Δ_g is needed to reproduce the HSE06 gap energy; we therefore denote this method PBE+U_d+Δ_g. With this PBE+U approach we can increase the density of the **k**-mesh to reveal details in the dielectric spectra.

4. Results

4.1. Sample preparation and phase analysis

The CTS deposition time was tuned in order to obtain relatively thin films for ellipsometry analysis (thickness after annealing: less than 100 nm). This approach has been demonstrated previously with other polycrystalline chalcogenide materials [24, 25], and it has been shown as an effective way to keep the surface roughness low, which reduces light scattering and depolarization effects. This makes it simpler to analyze the as-annealed films without the need of altering the original surface by polishing [13].

When analyzing a CTS film grown and annealed on Mo-coated glass rather than on bare glass, a few precautions should be taken. By annealing Mo in a S-containing atmosphere, both with and without a sulfide film deposited on top, it is well known that a MoS_2 layer is formed on top of the Mo layer if the temperature is high enough [26]. By means of Raman spectroscopy and x-ray photoemission spectroscopy (not shown), we have confirmed the presence of a MoS_2 layer up

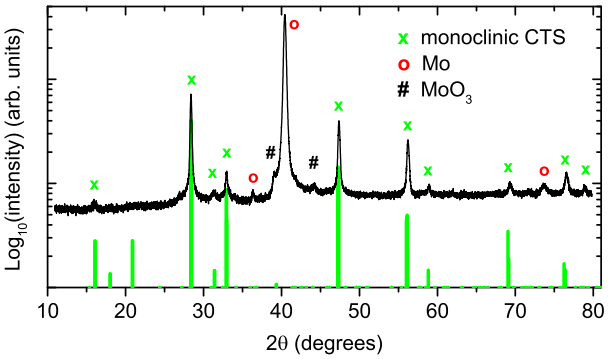

Figure 3: X-ray diffraction pattern of a 2 μm-thick CTS film prepared with the same recipe as the film for ellipsometry analysis. All detected peaks but two can be attributed to monoclinic Cu_2SnS_3 (green - JCPDS-01-070-6338) and cubic Mo (red - JCPDS-01-071-3771; the peak at 36.4° is the k_β component of the strongest Mo peak). The two remaining peaks are also present in the XRD pattern of the bare Mo film (not shown) and are attributed to two MoO_3 phases (black - JCPDS-01-076-1003 and JCPDS-01-089-1554). The reference powder pattern of monoclinic CTS is displayed in green below the measured XRD pattern.

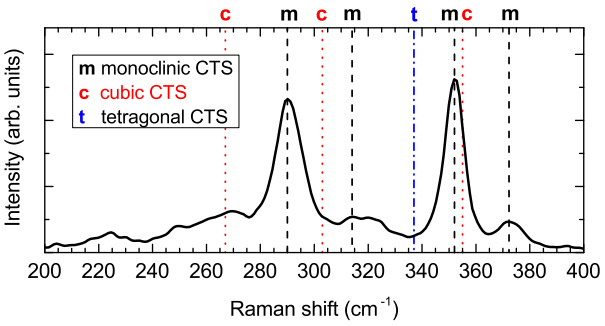

Figure 4: Averaged Raman spectrum of the annealed CTS films on a glass/Mo/MoS_2 stack from five measurement points. The dashed lines correspond to the four main peaks identified by Berg et al. [28] as vibrational modes of monoclinic CTS. The dotted and dash-dotted lines correspond to vibrational modes attributed by Fernandes et al. [27] to cubic and tetragonal CTS respectively.

to 100 nm thick in our samples after annealing. This layer is clearly visible when taking a cross-sectional SEM image (Fig. 2). Compositional analysis of such thin samples by EDX is inaccurate due to x-rays being generated in all the layers of the stack and due to the overlap of the Mo and S peaks in the X-ray spectrum. Therefore, thicker films (around 2 μm) were prepared using the same recipe and analyzed by EDX. The resulting atomic composition is Cu = (33.0 ± 0.3)%, Sn = (18.0 ± 0.1)%, S = (49.0 ± 0.3)% with Cu/Sn = 1.81 ± 0.02, similar to the composition of the best performing solar cells [1, 2].

To confirm that a CTS phase is actually formed in the bulk of the film, x-ray diffraction (XRD) was performed on the same thicker film used for EDX measurements to increase the signal intensity. The detected peaks that are not related to Mo or MoO_3 can be attributed to monoclinic CTS based on the reference pattern JCPDS-01-070-6338 (Fig. 3). Such peaks are related to different CTS crystal planes, thus we conclude that our CTS film does not have a unique crystal orientation perpendicular to the substrate.

It should be emphasized that distinguishing between different CTS polymorphs by means of XRD alone is a difficult task due to the similarity of their crystal structures and, hence, of their XRD patterns [4]. On the other hand, the Raman spectra of the different CTS polymorphs are more characteristic [27, 28]. Therefore, we performed Raman spectroscopy on five different spots in the vicinity of the ellipsometry measurement area and plotted the average spectrum (Fig. 4). Due to the presence of the four characteristic Raman peaks of monoclinic CTS [28] and to the absence of both cubic- and tetragonal CTS peaks [27], it can be concluded that monoclinic CTS is the main phase in the deposited film.

4.2. *Ellipsometry analysis*

To measure the dielectric function of the Mo layer independently, we annealed a single Mo film grown on soda lime glass in the same deposition run as the investigated CTS stack. The annealing conditions were the same as those used for the CTS stack, with the exception that no sulfur was added, and that a clean quartz tube was used in the annealing furnace. Annealing the Mo film prior to ellipsometry measurement was necessary because it was observed that the dielectric function of Mo changed noticeably when annealed. The thickness of the films (500 nm) and its large absorption coefficient allows to neglect reflection at the Mo-SLG interface and only consider reflection at the Mo-air interface. Hence, the unknown parameters were the thickness of the surface roughness layer and the dielectric function of Mo. The latter was fitted using literature spectra [29] as an initial guess. The results are shown in Fig. A.1, Appendix A. The mean square error of the fit is 2.834.

To measure the dielectric function of the MoS_2 layer, we annealed a Mo-coated glass substrate in a S atmosphere together with the CTS sample used for ellipsometry analysis. The dielectric function of Mo was treated as a known parameter, based on the previous measurement. On the other hand, the presence of the Mo-MoS_2 reflection makes it necessary to include the thickness of MoS_2 as a fitted parameter. The dielectric function of MoS_2 was fitted using literature spectra [26] as an initial guess. The mean square error of the fit is 3.362. Well-known excitonic features [30] are clearly visible in our measured dielectric function and are labeled in Fig. A.2, Appendix A. Even though single-crystal MoS_2 has an indirect band gap of about 1.2 eV [31], significant absorption occurs below the band gap energy in our film, as evident from the ε_2 spectrum in Fig. A.2, Appendix A. This has been observed before in multi-crystalline MoS_2 and has been attributed to defect absorption at surfaces [31].

Turning now to the full Mo/MoS_2/CTS layer stack of interest for this study, a relatively simple optical model was employed to fit ellipsometry data, in order to minimize the risk of obtaining artifacts in the dielectric function. The model (Fig. 5)

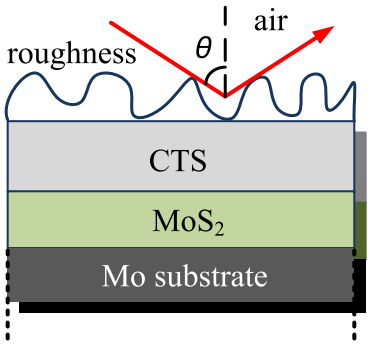

Figure 5: Optical model used for data analysis of ellipsometry measurements on CTS. It consists of a Mo bulk substrate, a MoS_2 layer, and a CTS layer. From an optical point of view, a bulk substrate is a layer in which only the reflection from the top surface is considered. All layers are assumed to be uniform in the depth direction and without intermixing. Bruggeman's effective medium theory is employed to treat the surface roughness layer. The angle of incidence of polarized light in the measurement is labeled as θ.

consists of a Mo bulk substrate, a MoS_2 layer, a CTS layer and a surface roughness layer. All layers are assumed to be uniform in the depth direction and without intermixing. Cross-sectional SEM images (Fig. 2) indeed show a regular CTS surface roughness layer (R_q = 9.5±0.5 nm by AFM) and no clearly visible intermixing between the layers, which qualitatively justifies our assumptions. When fitting the ellipsometry spectra, the dielectric functions of both Mo and MoS_2 were treated as known parameters, based on the previous measurements. The fitted parameters were the thicknesses of the MoS_2 and CTS layers, the surface roughness layer thickness, and the dielectric function of the CTS layer. In order to increase sensitivity for the double absorption onset, the node spacing of the b-spline model of the CTS dielectric function was decreased to 0.02 eV in the 0.8-1.1 eV spectral region. The measured and fitted Ψ and Δ spectra, with a mean square error of 2.936, are shown in Fig. A.3, Appendix A. The value of the error is regarded as acceptably low. In fact, simultaneous fitting of measurements with less than six incidence angles lowers the mean square error but it also yields less robust results and increases the correlation between the estimated parameters. The fitted thickness of CTS is 92.07 ± 0.09 nm and the resulting CTS dielectric function is shown in Fig. 6. Note that two absorption onsets exist, compatible with previous reports on monoclinic CTS [1, 5, 6].
The fitted value of the surface roughness layer R_e is 12.72 ± 0.03 nm. This is is good agreement with the value 14.6 nm predicted by the empirical formula $R_e \approx 1.5\,R_q + 4$ Å [15] using the value of R_q measured by AFM. Combined with the fact that our measured R_q is more than 10 times smaller than the minimum wavelength (210 nm) used in our ellipsometry measurement [13], this indicates that Bruggeman's effective medium theory is likely to be an acceptable method to treat the surface roughness layer in our analyzed sample.

Absorber layers in thin-film solar cells are normally made much thicker than our analyzed sample in order to allow full absorption of light and achieve larger crystal grains to facilitate electrical transport. However, the dielectric function is not expected to depend strongly on thickness as long as the film is crystalline [32] and the optical model employed for ellipsometry data analysis is correct [13]. In fact, throughout our experiments we observed significant distortion of the measured CTS dielectric function only for film thicknesses below 30 nm, due to partial loss of long-range order from partially amorphous structure, and above 150 nm, due to inaccurate modeling of surface roughness.

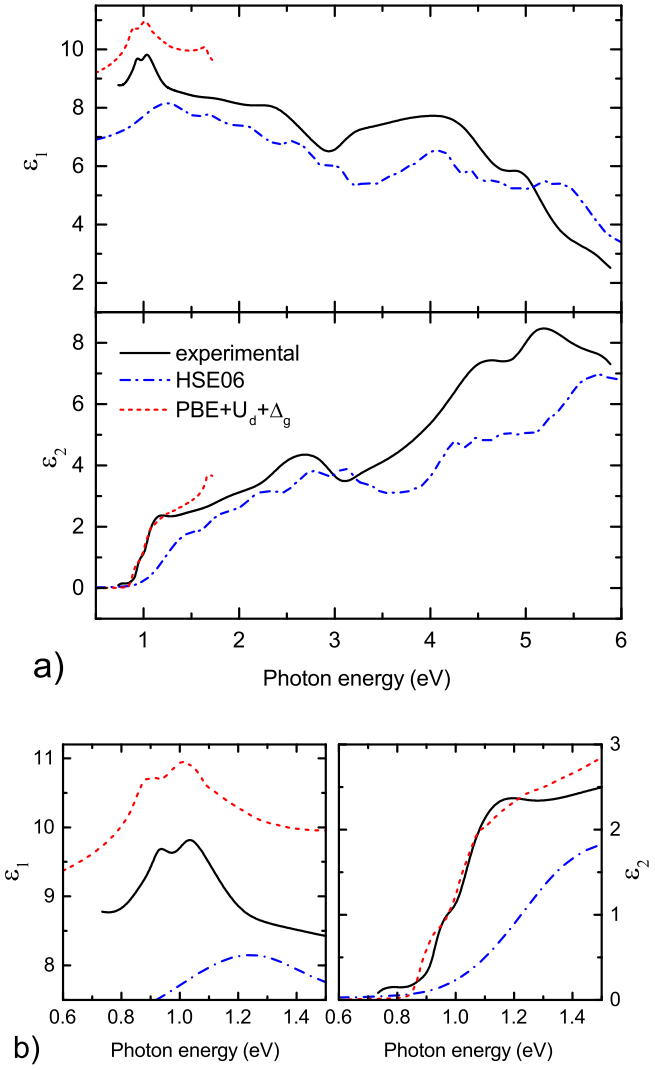

Figure 6: (a) Real and imaginary parts of the dielectric function $\varepsilon(E) = \varepsilon_1(E) + i\varepsilon_2(E)$ for of monoclinic CTS, as determined by experimental and computational techniques. Black solid line: experimental spectra by spectroscopic ellipsometry. Blue dash-dotted line: calculated spectra with the HSE06 approach with a $5\times5\times5$ **k**-mesh (N_k = 39 **k**-points). Red dashed line: calculated spectra with the PBE+U_d+Δ_g with a denser $30\times30\times30$ **k**-mesh (N_k = 6992 **k**-points). (b) Detailed view of the near-band-gap spectral region. Note that the clear double absorption onset observed experimentally is revealed by computation only in the case of the denser **k**-mesh.

4.3. Electronic structure calculation

From the calculated electronic structure of monoclinic CTS, we observe a direct Γ-point band gap with the gap energy

E_g = 0.83 eV. Similar theoretical results have been reported before: Zhai et al. [4] reported 0.84 eV also with the HSE functional, Shigemi et al. [11] got 0.88 eV using HSE with a larger Hartree-Fock exchange contribution, and Zawadzki et al. [9] found 0.63 eV with a beyond-DFT GW approach. Overall, these theoretical calculations [4, 9, 10, 11] yield similar electronic band structure and/or density-of-states. Moreover, calculation of monoclinic Cu_2SnSe_3 by Choi et al. [33] with HSE showed improved dielectric response with a denser **k**-mesh. However, none of the earlier published works discusses any feature in the electronic structure that can explain a double onset phenomenon.

Computation of the dielectric function from HSE06 yields spectra that are overall in fairly good agreement with the experimental results in the whole energy region (Fig. 6). However, one observes that the calculated spectrum of $\varepsilon_2(E)$ has a weaker response just above the band gap energy. Also the peak at around 1.2 eV in the calculated $\varepsilon_1(E)$ spectrum is too small, too broad, and shifted to higher energies. These HSE06 calculations were done with a **k**-mesh of $K = 5 \times 5 \times 5$ (implying 39 **k**-points in the IBZ). Such **k**-mesh is commonly used, and it is usually dense enough to generate accurate total energy and an overall good electron density for semiconductors. However, in order to see details in the optical properties, a much denser mesh is needed. We therefore use the PBE+U_d+Δ_g method with correction of the Cu d-states and an additional constant upwards shift Δ_g = 0.52 eV of the CBM to reproduce the HSE06 band gap energy. With this method we increase the **k**-mesh until the details of $\varepsilon_2(E)$ are revealed. We find an improved $\varepsilon_2(E)$ spectrum between E_g and E_g + 0.5 eV for a **k**-mesh of $K = 30 \times 30 \times 30$ (6992 **k**-points; red dotted line in Fig. 6). Two significant details are observed: first, the strength of the response function is much larger in this low-energy region and therefore the spectrum shows a strong absorption onset. Second, the double onset becomes visible. Both of these features are in very good agreement with the measured spectrum of $\varepsilon_2(E)$. With the improved $\varepsilon_2(E)$ spectrum for the low-energy region, also the real part of the dielectric function is improved considerably below E_g + 0.5 eV. The main peak in $\varepsilon_1(E)$ now has a reasonable size and width, but is also correctly shifted to around 1.0 eV. Moreover, one observes that this peak is actually a double peak, which also is in agreement with the measured spectrum.

For CTS, as for similar photovoltaic materials, it is well known that the regular PBE generates zero, or almost zero, gap energy. That implies also that the band edges become somewhat distorted. The d-state correction in PBE+U is important not only to correct those orbitals but also to open the gap to 0.31 eV. Although a still too small gap energy, that is enough to describe the curvatures of the bands much better. In order to verify that the PBE+U method does not involve an incorrect model of the interaction potential, we analyze the computational method for monoclinic Cu_2SiS_3 (CSS). This compound is similar to CTS, however with a much larger gap ($E_g \approx 2.6$ eV)[34] and the regular PBE potential can therefore be used. In Fig. A.4, Appendix A, we demonstrate that both the regular PBE method and the PBE+U method generate similar dielectric response spectra $\varepsilon_2(E)$ as HSE06 for the sparse **k**-mesh of $K = 5 \times 5 \times 5$, although both methods have slightly larger responses than HSE06. Increasing the **k**-mesh improves the $\varepsilon_2(E)$ spectrum correspondingly for both PBE and PBE+U. Moreover, we find that also monoclinic CSS exhibits a double absorption onset similar to CTS.

Thus, the calculation confirms that monoclinic CTS has a strong dielectric response for photons with energies just above the gap energy, and that the compound exhibits a double absorption onset.

5. Discussion

As demonstrated in Fig. 7, the calculation predicts that the dielectric function of monoclinic CTS is very anisotropic in the near-band gap region. In the very low energy region ($E_g \leq E < E_g$ + 0.15 eV) the polarization in the z-direction is completely dominating, while for higher photon energies also the polarization in the y-direction (and partly the x-direction) contributes to the dielectric response. See Fig. 7 for definition of crystal orientation.

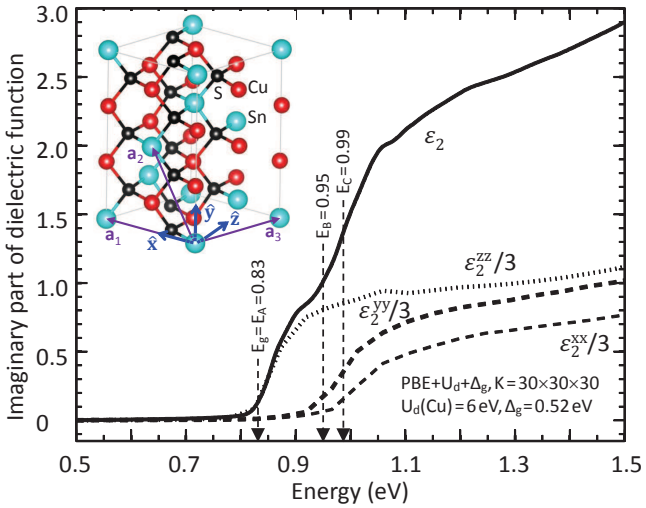

Figure 7: Polarization dependency of the dielectric function of CTS with the PBE+U_d+Δ_g computational approach. The calculated dielectric response $\varepsilon_2(E)$ is very anisotropic in the near-band-gap spectral region. The primitive cell of the crystal is defined by the lattice vectors $\mathbf{a}_1$, $\mathbf{a}_2$, and $\mathbf{a}_3$, and the orientation of the polarization is described in the Cartesian coordinate space ($\hat{\mathbf{x}}$, $\hat{\mathbf{y}}$, $\hat{\mathbf{z}}$).

To explain these features, we analyze in Fig. 8 the electronic structure more in detail. One first observes the direct gap at the Γ-point. This gap energy between VBM (for band v_1) and CBM (for band c_1) is directly associated to the first absorption onset. The second and third uppermost valence bands (v_2 and v_3) have maxima also at the Γ-point, with the energies 0.12 and 0.16 eV below the VBM. These two bands are thus responsible for the second absorption onset. The three Γ-point transition energies are thus $E_A = E_g$ (equal to 0.83 eV in the HSE06 calculation), $E_B = E_g$ + 0.12 eV (or 0.95 eV), and $E_C = E_g$ + 0.16 eV (or 0.99 eV). One notices that the topmost valence band is very flat along the (010) direction (and also along the (100)

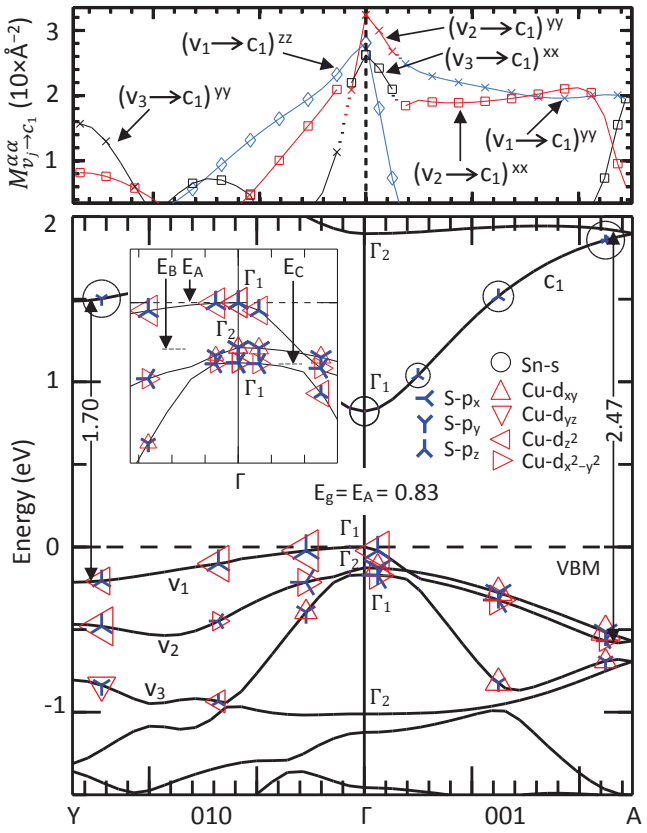

Figure 8: Electronic band structure of monoclinic CTS along two main symmetry directions, computed with the HSE06 potential. At the Γ-point VBM, there are three close-lying valence bands (see inset figure) that contribute to the observed double absorption onset near the band gap energy. The marks indicate the main character of the energy states. The upper panel shows the optical interband matrix elements for electric dipole induced transitions. Each line color refers to a specific valence band for the transition $v_j \to c_1$, and each marker type refers to a specific polarization of the matrix element $M^{\alpha\alpha}$. Blue, red, and black lines represent transitions from the uppermost (v_1), the second uppermost (v_2), and the third uppermost (v_3) valence bands, respectively, to the lowest conduction band (c_1). Square, cross, and diamond markers represent x-, y-, and z-polarized transitions respectively.

direction; not displayed). Therefore, the absorption coefficient can be large near the gap energy, i.e., for $E_g \le E < E_g + 0.5$ eV. The direct energy gap at the Y-point is only 1.70 eV = E_g + 0.87 eV, and the corresponding energy at the A-point is 2.47 eV = E_g + 1.64 eV. Optical transitions at these **k**-states generate the peaks in the dielectric function for energies from 1.8 to 2.5 eV. However, also **k**-states in other directions in the IBZ contribute to the spectrum in this energy range. For instance, the energy between the VBM and the second lowest conduction band is only 1.90 eV at the Γ-point.

The energy state at the CBM has the irreducible representation Γ_1 of C_2 point group. Also the VBM energy state has Γ_1 symmetry. The irreducible representations describe the allowed polarization of the allowed electric dipole induced transitions for that **k**-state. The lowest conduction band has a strong contribution of Sn s-like character. The conduction band contains also S p_y-like (S p_z-like) character along the (010) direction ((001) direction). Furthermore, the uppermost valence band has primarily Cu d_{z^2}-like and S p_z-like character. This explains the strong and in-plane z-polarized dielectric response related to the first absorption onset. The second uppermost valence band has Γ_2 symmetry at its maximum with primarily Cu d_{xy}-like and S p_y-like character, while the third band has Γ_1 symmetry at its maximum with primarily Cu $d_{x^2-y^2}$-like and S p_x-like character. Transitions from these two valence bands yield the pronounced x- and y-polarized dielectric response. Of the three topmost bands it is the third band that has most Sn s-like character away from the Γ-point, but the contribution is small (not displayed). Noticeably, along the (001) direction, the topmost valence bands (with Γ_1 symmetry at the VBM) and second valence band (with Γ_2 symmetry) cross about 18% away from the Γ-point, while the third band (with Γ_1 symmetry) "interacts" and bends downwards. At the cross-over point, the characters of the valence bands change symmetry, an effect which is typical for these types of band-band interactions.

The characters of the valence band states explain the optical transitions. In the top panel in Fig. 8, we present the optical matrix elements $M^{\alpha\alpha}_{v_j\to c_1} = |\langle\psi_{\mathbf{k}_{c_1}}|\hat{p}_\alpha\psi_{\mathbf{k}_{v_j}}\rangle|^2$, describing probability for optical transitions from the valence band v_j to the conduction band c_1. Note that here v_1 is the topmost valence state for each **k**-point, whether or not bands cross along the symmetry lines. One observes that close to the Γ-point the transitions from the topmost valence band (blue lines) have mainly $M^{zz}_{v_1\to c_1}$ contribution. The other terms in the optical matrix are less than 0.03, and therefore not presented in the figure. Transitions from the second valence band (red lines) have mainly $M^{yy}_{v_2\to c_1}$ contribution, while transitions from the third valence band (black lines) have mainly $M^{xx}_{v_3\to c_1}$ contribution. It is also clear how the character of the band states affects the contribution of $M^{\alpha\alpha}_{v_j\to c_1}$ when a band crosses or interacts with another band. The character of the bands, and the corresponding optical matrix elements, are the origin of the anisotropy of the dielectric function $\varepsilon_2(E)$ spectrum, and it also may explain why the double onset phenomenon is so pronounced in monoclinic CTS.

Unfortunately, the strong polarization dependence of the calculated dielectric response of monoclinic CTS cannot be cross-checked experimentally in this work. The reason is that the crystal grains in our CTS film are not oriented along a single lattice direction, as is evident by the number of different peaks observed in the XRD pattern in Fig. 3. A spectroscopic ellipsometry measurement on a (001) surface in monoclinic CTS is needed to observe experimentally the polarization-dependent absorption onset.

Nevertheless, the shape of the dielectric function, the energy of the first absorption onset and the energy separation of the two onsets can be compared between experiment and theory. In general, the band gap of a crystalline direct semiconductor can be estimated experimentally by extrapolation of the linear region above the absorption onset in an $(\alpha En)^2$ versus E plot, where α and n are the absorption coefficient and refractive index of the material, and E is the photon energy [35]. Often, $(\alpha E)^2$ plots are used for this purpose in unpolarized transmission and reflection measurements because n is not easily derived from the measurement. However, it has been shown that band gap estimation can be difficult if n is omitted in the plot

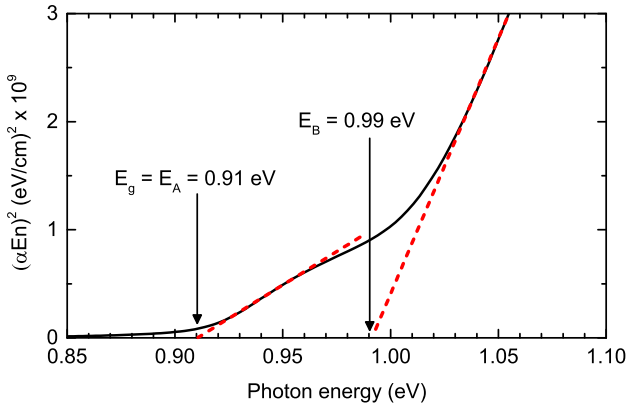

Figure 9: $(\alpha En)^2$ versus E plot for monoclinic CTS, where the distance between the initial and final state of the two optical transitions responsible for the double absorption onset can be estimated from the linear regions of the plots. The absorption coefficient α and the refractive index n are derived from the experimentally determined dielectric function of monoclinic CTS.

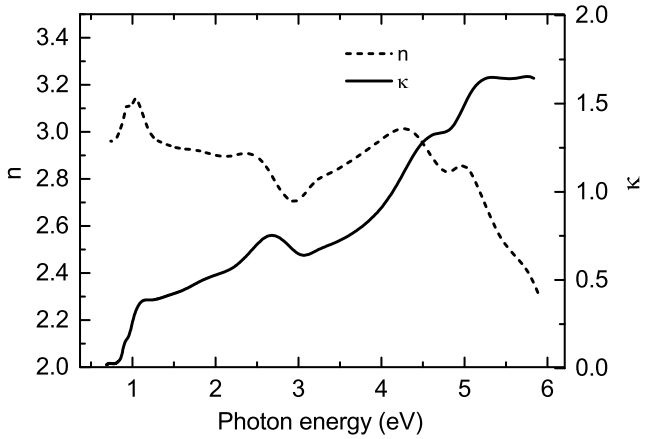

Figure 10: Refractive index n and extinction coefficient κ for monoclinic CTS, derived by the experimental dielectric function spectra obtained by spectroscopic ellipsometry. The refractive index exhibits relatively low dispersion in the visible region of light.

[29]. In the case of an ellipsometry measurement, α and n can be readily extracted from the measured dielectric function of CTS by employing the standard relations $\varepsilon_1 = n^2 - \kappa^2$, $\varepsilon_2 = 2n\kappa$, and $\alpha = 4\pi\kappa E/hc$, where κ is the extinction coefficient, h is Planck's constant and c is the speed of light in vacuum. Then, the distance between the initial and final state of the two direct transitions involved in the double onset can be estimated. This method yields $E_A = E_g = 0.91 \pm 0.01$ eV for the first onset and $E_B = 0.99 \pm 0.01$ eV for the second onset in monoclinic CTS (Fig. 9). The energy difference between the two onsets is therefore 0.12 eV by theory and 0.08 eV ± 0.01 eV by experiment. Then, the double-onset phenomenon observed experimentally can indeed be explained as caused by optical transitions from the three topmost bands at the VBM in a perfectly crystalline monoclinic CTS. The phenomenon does thus not need to be due to structural imperfections, like inclusion of disordered structures or secondary phases.

As for the energy of the first absorption onset, the HSE06 calculation predicts $E_A = E_g = 0.83$ eV, whereas the measurement yields $E_A = E_g = 0.91 \pm 0.1$ eV. It must be emphasized that the calculated value is obtained from the single-particle energies at the band edges, and one shall not expect that this Kohn-Sham gap energy be exactly equal to the true fundamental band gap energy. From similar calculations of CIGS and CZTS [19, 20] we expect the HSE06 method to underestimate the actual band gap energy by about 0.1-0.2 eV.

Regarding the shape of the dielectric function, it shall be emphasized that only with a fine **k**-point sampling the shapes of both the real and imaginary parts of the computed dielectric function are improved considerably in the low energy region (i.e, for photon energies between 0 and E_g + 1.5 eV). Considering this, the computed dielectric response spectra are in good agreement with the experimental spectra from monoclinic CTS in the whole energy region from 0.7 to 5.9 eV. Based on the experimental spectra, the refractive index n of monoclinic CTS is between 2.7 and 3.2 over a broad spectral region, from below the band gap to about 5 eV (Fig. 10). Finally, we note that the absorption coefficient of monoclinic CTS is quite large in the spectral region of large solar irradiance (roughly 1.0-2.5 eV), when compared to the widely investigated chalcogenide thin film absorbers for photovoltaics CIGS, CdTe, and CZTS (Fig. 11). In particular, the near-band gap region between 1.0 and 1.5 eV features very strong absorption due to the contributions from multiple optical transitions, even when compared to similar low band gap materials such as CZTSe. This has two beneficial consequences: 1) the absorber layer can be thinner, resulting in lower material consumption, and 2) charge carriers are, on the average, generated closer to the p-n junction, where the collection probability is high. These features, together with the relatively low band gap, make CTS a promising candidate as a bottom absorber in tandem solar cells.

6. Conclusion

We have experimentally determined the dielectric function of monoclinic CTS by spectroscopic ellipsometry from 0.7 to 5.9 eV. An experimental procedure has been proposed to overcome the challenges of extracting the dielectric function of a CTS thin film grown on a glass/Mo substrate. This involves separate measurement of the dielectric function of each layer in the stack, and careful initialization of the unknown parameters in the data fitting step using the results from other measurement techniques. The experimental dielectric function has been compared to that obtained by computation using DFT with a satisfactory agreement also at a quantitative level. The calculation has confirmed a double absorption onset at 0.9-1.0 eV, which originates from direct optical transitions at the Γ-point from three energetically closely-spaced valence bands to a single conduction band in perfectly crystalline monoclinic CTS bulk. Thus, the phenomenon does not need to be due to structural imperfections, like inclusion of disordered structure or secondary phases. Importantly, the double onset can only be

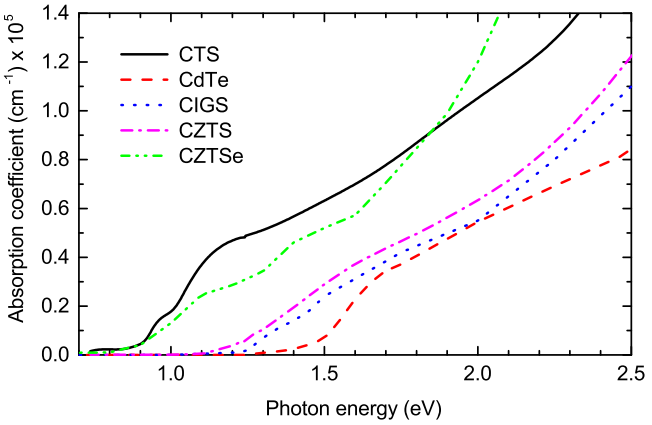

Figure 11: Absorption coefficient of different chalcogenide absorbers in the spectral region of most interest for solar cells. CTS: derived from the dielectric function measured in this work; CdTe: taken from Li et al. [36]; CIGS ($CuIn_{0.62}Ga_{0.38}Se_2$): taken from Minoura et al. [24]; CZTS (Cu_2SnZnS_4): taken from Li et al. [25]; CZTSe ($Cu_2SnZnSe_4$), taken from Choi et al. [37]. The absorption onset in CTS is relatively sharp and with a high intensity, even when compared to CZTSe, which has a similar band gap.

predicted in the case of using a dense **k**-mesh. We therefore use the PBE+U approach (with dense **k**-mesh, to reveal details in the dielectric function spectra) combined with the HSE06 hybrid functional (for better description of the overall spectra) to describe the optical properties. The calculation predicts that the response function of CTS is very polarization dependent near the band gap energy, and this will help future optical analysis of monocrystalline CTS samples. Finally, we note that the absorption coefficient of monoclinic CTS is particularly large in the near-band-gap region between 1.0 and 1.5 eV. This makes CTS an interesting option as a bottom absorber in tandem solar cells.

Acknowledgements

The experimental work was supported by a grant from the Danish Council for Strategic Research. CINF is funded by the Danish National Research Foundation (DNRF54). The theoretical work was supported by the Research Council of Norway (project 243642), with the access to the computer centers NSC and USIT for high-performance computing resources via SNIC and NOTUR. A.C. is grateful to Maksym Plakhotnyuk and to the Nanocarbon group at DTU Nanotech for help with AFM measurements and usage of the Raman setup, respectively.

References

[1] M. Nakashima, J. Fujimoto, T. Yamaguchi, M. Izaki, Cu_2SnS_3 thin-film solar cells fabricated by sulfurization from NaF/Cu/Sn stacked precursor, Applied Physics Express 8 (4) (2015) 042303. doi:10.7567/APEX.8.042303.

[2] A. Kanai, K. Toyonaga, K. Chino, H. Katagiri, H. Araki, Fabrication of Cu_2SnS_3 thin-film solar cells with power conversion efficiency of over 4%, Japanese Journal of Applied Physics 54 (8S1) (2015) 08KC06. doi:10.7567/JJAP.54.08KC06.

[3] L. L. Baranowski, P. Zawadzki, S. Christensen, D. Nordlund, S. Lany, A. C. Tamboli, L. Gedvilas, D. S. Ginley, W. Tumas, E. S. Toberer, A. Zakutayev, Control of Doping in Cu_2SnS_3 through Defects and Alloying, Chemistry of Materials 26 (17) (2014) 4951–4959. doi:10.1021/cm501339v.

[4] Y.-T. Zhai, S. Chen, J.-H. Yang, H.-J. Xiang, X.-G. Gong, A. Walsh, J. Kang, S.-H. Wei, Structural diversity and electronic properties of Cu_2SnX_3 (X = S, Se): A first-principles investigation, Physical Review B 84 (7) (2011) 075213. doi:10.1103/PhysRevB.84.075213.

[5] N. Aihara, A. Kanai, K. Kimura, M. Yamada, K. Toyonaga, H. Araki, A. Takeuchi, H. Katagiri, Sulfurization temperature dependences of photovoltaic properties in Cu_2SnS_3-based thin-film solar cells, Japanese Journal of Applied Physics 53 (5S1) (2014) 05FW13. doi:10.7567/JJAP.53.05FW13.

[6] D. M. Berg, R. Djemour, L. Gütay, G. Zoppi, S. Siebentritt, P. J. Dale, Thin film solar cells based on the ternary compound Cu_2SnS_3, Thin Solid Films 520 (19) (2012) 6291–6294. doi:10.1016/j.tsf.2012.05.085.

[7] J. de Wild, E. V. C. Robert, B. El Adib, P. J. Dale, Optical characterization of solution prepared Cu_2SnS_3 for photovoltaic applications, MRS Proceedings 1771 (2015) mrss15–2135683. doi:10.1557/opl.2015.624.

[8] L. L. Baranowski, K. McLaughlin, P. Zawadzki, S. Lany, A. Norman, H. Hempel, R. Eichberger, T. Unold, E. S. Toberer, A. Zakutayev, Effects of disorder on carrier transport in Cu_2SnS_3, arXiv:1504.01327arXiv:1504.01327.

[9] P. Zawadzki, L. L. Baranowski, H. Peng, E. S. Toberer, D. S. Ginley, W. Tumas, A. Zakutayev, S. Lany, Evaluation of photovoltaic materials within the Cu-Sn-S family, Applied Physics Letters 103 (25) (2013) 253902. doi:10.1063/1.4851896.

[10] L. Xi, Y. B. Zhang, X. Y. Shi, J. Yang, X. Shi, L. D. Chen, W. Zhang, J. Yang, D. J. Singh, Chemical bonding, conductive network, and thermoelectric performance of the ternary semiconductors Cu_2SnX_3 (X = Se, S) from first principles, Physical Review B 86 (15) (2012) 155201. doi:10.1103/PhysRevB.86.155201.

[11] A. Shigemi, T. Maeda, T. Wada, First-principles calculation of Cu_2SnS_3 and related compounds, Physica Status Solidi (B) 252 (6) (2015) 1230–1234. doi:10.1002/pssb.201400346.

[12] D. Tiwari, T. K. Chaudhuri, T. Shripathi, U. Deshpande, V. G. Sathe, Structural and optical properties of layer-by-layer solution deposited Cu_2SnS_3 films, Journal of Materials Science: Materials in Electronics 25 (9) (2014) 3687–3694. doi:10.1007/s10854-014-2076-y.

[13] H. Fujiwara, Spectroscopic Ellipsometry - Principles and Applications, Chapter 5, Wiley, 2007.

[14] A. Crovetto, A. Cazzaniga, R. B. Ettlinger, J. Schou, O. Hansen, Optical properties and surface characterization of pulsed laser-deposited Cu_2ZnSnS_4 by spectroscopic ellipsometry, Thin Solid Films 582 (2015) 203–207. doi:10.1016/j.tsf.2014.11.075.

[15] J. Koh, Y. Lu, C. R. Wronski, Y. Kuang, R. W. Collins, T. T. Tsong, Y. E. Strausser, Correlation of real time spectroellipsometry and atomic force microscopy measurements of surface roughness on amorphous semiconductor thin films, Applied Physics Letters 69 (9) (1996) 1297. doi:10.1063/1.117397.

[16] G. Kresse, D. Joubert, From ultrasoft pseudopotentials to the projector augmented-wave method, Physical Review B 59 (3) (1999) 1758–1775. doi:10.1103/PhysRevB.59.1758.

[17] G. Kresse, J. Furthmüller, Efficient iterative schemes for ab initio total-energy calculations using a plane-wave basis set, Physical Review B 54 (16) (1996) 11169–11186. doi:10.1103/PhysRevB.54.11169.

[18] J. Heyd, G. E. Scuseria, M. Ernzerhof, Hybrid functionals based on a screened Coulomb potential, The Journal of Chemical Physics 118 (18) (2003) 8207. doi:10.1063/1.1564060.

[19] L. E. Oikkonen, M. G. Ganchenkova, A. P. Seitsonen, R. M. Nieminen, Vacancies in $CuInSe_2$: new insights from hybrid-functional calculations., Journal of Physics: Condensed Matter 23 (42) (2011) 422202. doi:10.1088/0953-8984/23/42/422202.

[20] H. Zhao, C. Persson, Optical properties of Cu(In,Ga)Se_2 and $Cu_2ZnSn(S,Se)_4$, Thin Solid Films 519 (21) (2011) 7508–7512.

[21] J. P. Perdew, K. Burke, M. Ernzerhof, Generalized Gradient Approximation Made Simple, Physical Review Letters 77 (18) (1996) 3865–3868. doi:10.1103/PhysRevLett.77.3865.

[22] V. I. Anisimov, J. Zaanen, O. K. Andersen, Band theory and Mott insulators: Hubbard U instead of Stoner I, Physical Review B 44 (3) (1991)

943–954. doi:10.1103/PhysRevB.44.943.
[23] C. Persson, C. Dong, L. Vayssieres, A. Augustsson, T. Schmitt, M. Mattesini, R. Ahuja, J. Nordgren, C. Chang, A. Ferreira da Silva, J.-H. Guo, X-ray absorption and emission spectroscopy of ZnO nanoparticle and highly oriented ZnO microrod arrays, Microelectronics Journal 37 (8) (2006) 686–689. doi:10.1016/j.mejo.2005.12.009.
[24] S. Minoura, K. Kodera, T. Maekawa, K. Miyazaki, S. Niki, H. Fujiwara, Dielectric function of Cu(In,Ga)Se_2-based polycrystalline materials, Journal of Applied Physics 113 (6) (2013) 063505. doi:10.1063/1.4790174.
[25] J. Li, H. Du, J. Yarbrough, A. Norman, K. Jones, G. Teeter, F. L. Terry, D. Levi, Spectral optical properties of Cu_2ZnSnS_4 thin film between 0.73 and 6.5 eV., Optics Express 20 (102) (2012) A327–A332. doi:10.1364/OE.20.00A327.
[26] C. Yim, M. O'Brien, N. McEvoy, S. Winters, I. Mirza, J. G. Lunney, G. S. Duesberg, Investigation of the optical properties of MoS_2 thin films using spectroscopic ellipsometry, Applied Physics Letters 104 (10) (2014) 103114. doi:10.1063/1.4868108.
[27] P. A. Fernandes, P. M. P. Salomé, A. F. da Cunha, Cu_xSnS_{x+1} (x = 2, 3) thin films grown by sulfurization of metallic precursors deposited by dc magnetron sputtering, Physica Status Solidi (C) 7 (2010) 901–904. doi:10.1002/pssc.200982746.
[28] D. M. Berg, R. Djemour, L. Gütay, S. Siebentritt, P. J. Dale, X. Fontane, V. Izquierdo-Roca, A. Pérez-Rodriguez, Raman analysis of monoclinic Cu_2SnS_3 thin films, Applied Physics Letters 100 (19) (2012) 192103. doi:10.1063/1.4712623.
[29] S. Marsillac, N. Barreau, H. Khatri, J. Li, D. Sainju, A. Parikh, N. J. Podraza, R. W. Collins, Spectroscopic ellipsometry studies of In_2S_3 top window and Mo back contacts in chalcopyrite photovoltaics technology, Physica Status Solidi (C) 5 (5) (2008) 1244–1248. doi:10.1002/pssc.200777889.
[30] R. A. Neville, B. L. Evans, The Band Edge Excitons in 2H–MoS_2, Physica Status Solidi (B) 73 (2) (1976) 597–606. doi:10.1002/pssb.2220730227.
[31] C. B. Roxlo, R. R. Chianelli, H. W. Deckman, A. F. Ruppert, P. P. Wong, Bulk and surface optical absorption in molybdenum disulfide, Journal of Vacuum Science & Technology A: Vacuum, Surfaces, and Films 5 (4) (1987) 555. doi:10.1116/1.574671.
[32] J. Tauc, R. Grigorovici, A. Vancu, Optical properties and electronic structure of amorphous germanium, Physica Status Solidi (B) 15 (2) (1966) 627–637. doi:10.1002/pssb.19660150224.
[33] S. G. Choi, J. Kang, J. Li, H. Haneef, N. J. Podraza, C. Beall, S.-H. Wei, S. T. Christensen, I. L. Repins, Optical function spectra and bandgap energy of Cu_2SnSe_3, Applied Physics Letters 106 (4) (2015) 043902. doi:10.1063/1.4907202.
[34] K. Toyonaga, H. Araki, Preparation and characterization of $Cu_2Si_xSn_{1-x}S_3$, Physica Status Solidi (C) 12 (6) (2015) 753–756. doi:10.1002/pssc.201400296.
[35] F. Stern, Elementary Theory of the Optical Properties of Solids, Solid State Physics 15 (1963) 299–408.
[36] J. Li, J. Chen, M. N. Sestak, C. Thornberry, R. W. Collins, Spectroscopic ellipsometry studies of thin film CdTe and CdS: From dielectric functions to solar cell structures, in: 2009 34th IEEE Photovoltaic Specialists Conference (PVSC), IEEE, 2009, pp. 001982–001987. doi:10.1109/PVSC.2009.5411520.
[37] S. G. Choi, H. Y. Zhao, C. Persson, C. L. Perkins, A. L. Donohue, B. To, A. G. Norman, J. Li, I. L. Repins, Dielectric function spectra and critical-point energies of $Cu_2ZnSnSe_4$ from 0.5 to 9.0 eV, Journal of Applied Physics 111 (3) (2012) 033506. doi:10.1063/1.3681814.

Appendix A. Supplementary figures

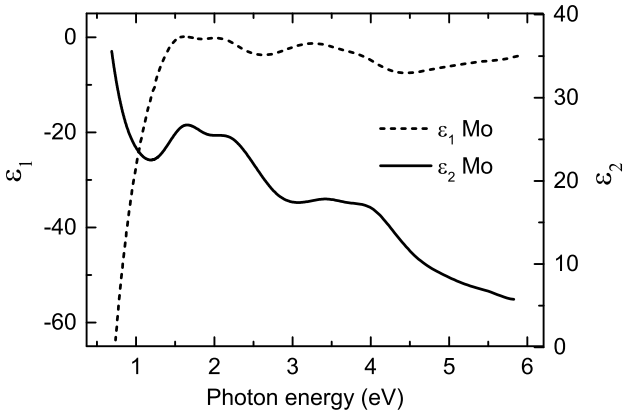

Figure A.1: Real and imaginary parts of the dielectric function $\varepsilon(E) = \varepsilon_1(E) + i\varepsilon_2(E)$ of the Mo layer from spectroscopic ellipsometry. The analyzed sample is a Mo film on glass after a 570°C anneal in N_2 without sulfur addition.

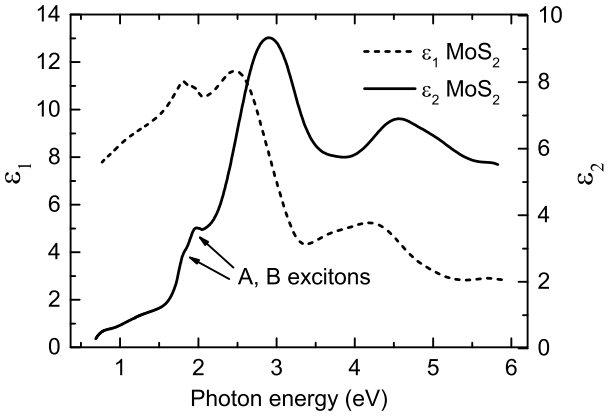

Figure A.2: Real and imaginary parts of the dielectric function $\varepsilon(E) = \varepsilon_1(E) + i\varepsilon_2(E)$ of the MoS_2 layer from spectroscopic ellipsometry. The analyzed sample is a Mo film on glass after a 570°C anneal in N_2 with 200 mg of sulfur, resulting in the formation of a MoS_2 layer at the surface, with a thickness of about 70 nm. Weak excitonic features, arising from direct d-d transitions split by spin-orbit interaction, are resolved and labeled A and B as in previous works [30].

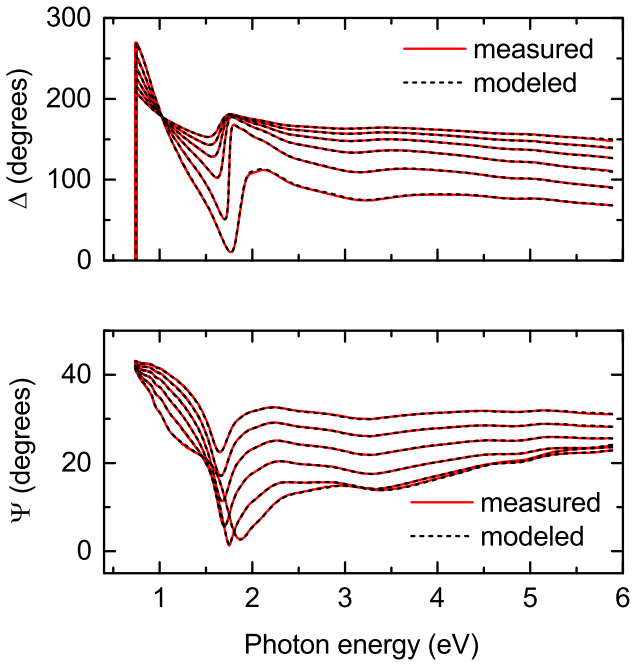

Figure A.3: Spectral magnitude $\Psi(E)$ and phase $\Delta(E)$ of the ratio between p- and s- type polarization reflection coefficients, measured on the glass/Mo/MoS_2/CTS stack by spectroscopic ellipsometry. For both $\Psi(E)$ and $\Delta(E)$, the measured and modeled spectra are shown at six angles of incidence, between 45° and 70°.

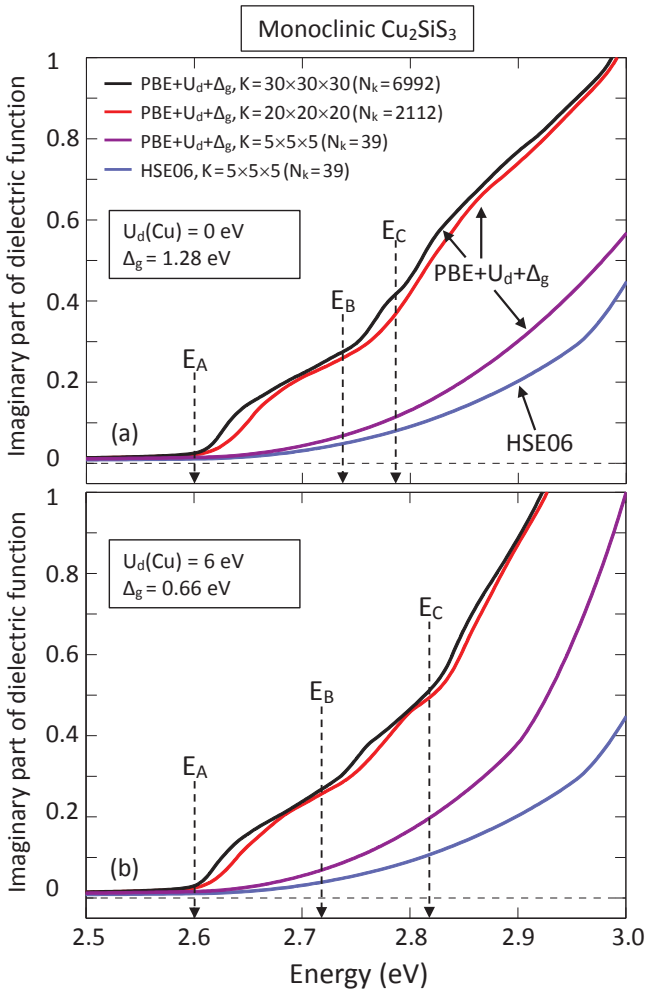

Figure A.4: The imaginary part ε_2 of the dielectric function for monoclinic Cu_2SiS_3 with the HSE06 and PBE+U_d+Δ_g computational approaches. All spectra has the onset at $E_g = E_A = 2.60$ eV, determined from a HSE06 calculation. First, we demonstrate that the PBE+Δ_g [i.e., with no onsite Coulomb potential, thus U_d(Cu)= 0 eV; see (a)] generates qualitatively the same near-gap spectra as PBE+U_d+Δ_g [with U_d(Cu)= 6 eV; see (b)] near the band-edge energy. Second, with a sparse $5\times5\times5$ **k**-mesh (implying $N_k = 39$ **k**-points in the IBZ) both HSE06 (light blue lines) and PBE+U_d+Δ_g (purple lines) show qualitatively the same spectra with no indication of a double onset near E_g. Third, with a denser $20\times20\times20$ **k**-mesh (2121 **k**-points; red lines) and $30\times30\times30$ **k**-mesh (6992 **k**-points; black lines) the double onset is clear, and one actually observes the contributions from the three transitions $E_A = 2.60$ eV, $E_B = 2.76$ eV, and $E_C = 2.83$ eV; compare with Fig. 7.